



## The value of distributed high-resolution UAV-borne observations of water surface elevation for river management and hydrodynamic modeling

Jiang, Liguang; Bandini, Filippo; Smith, Ole ; Jensen, Inger Klint; Bauer-Gottwein, Peter

*Published in:*  
Remote Sensing

*Link to article, DOI:*  
[10.3390/rs12071171](https://doi.org/10.3390/rs12071171)

*Publication date:*  
2020

*Document Version*  
Publisher's PDF, also known as Version of record

[Link back to DTU Orbit](#)

*Citation (APA):*  
Jiang, L., Bandini, F., Smith, O., Jensen, I. K., & Bauer-Gottwein, P. (2020). The value of distributed high-resolution UAV-borne observations of water surface elevation for river management and hydrodynamic modeling. *Remote Sensing*, 12(7), Article 1171. <https://doi.org/10.3390/rs12071171>

---

### General rights

Copyright and moral rights for the publications made accessible in the public portal are retained by the authors and/or other copyright owners and it is a condition of accessing publications that users recognise and abide by the legal requirements associated with these rights.

- Users may download and print one copy of any publication from the public portal for the purpose of private study or research.
- You may not further distribute the material or use it for any profit-making activity or commercial gain
- You may freely distribute the URL identifying the publication in the public portal

If you believe that this document breaches copyright please contact us providing details, and we will remove access to the work immediately and investigate your claim.

Article

# The Value of Distributed High-Resolution UAV-Borne Observations of Water Surface Elevation for River Management and Hydrodynamic Modeling

Liguang Jiang <sup>1,\*</sup>, Filippo Bandini <sup>1</sup>, Ole Smith <sup>2</sup>, Inger Klint Jensen <sup>2</sup>  
and Peter Bauer-Gottwein <sup>1</sup>

<sup>1</sup> Department of Environmental Engineering, Technical University of Denmark, 2800 Kgs. Lyngby, Denmark; fban@env.dtu.dk (F.B.); pbau@env.dtu.dk (P.B.G.)

<sup>2</sup> Orbicon, A/S, Høje-Taastrup, Linnés Allé 2, 2630 Taastrup, Denmark; osmi@orbicon.dk (O.S.); ikje@orbicon.dk (I.K.J.)

\* Correspondence: ljia@env.dtu.dk

Received: 19 March 2020; Accepted: 4 April 2020; Published: 6 April 2020



**Abstract:** Water level or water surface elevation (WSE) is an important state variable of rivers, lakes, and wetlands. Hydrodynamic models of rivers and streams simulate WSE and can benefit from spatially distributed WSE observations, to increase model reliability and predictive skill. This has been partially addressed by satellite radar altimetry, but satellite altimetry is unable to deliver useful data for small rivers. To overcome such limitations, we deployed a radar altimetry system on an unmanned aerial vehicle (UAV), to map spatially distributed WSE. We showed that UAV altimetry can provide observations of WSE with a very high spatial resolution (ca. 0.5 m) and accuracy (ca. 3 cm), in a time-saving and cost-effective way. Furthermore, we investigated the value of this dataset for the calibration and validation of hydrodynamic models. Specifically, we introduced spatially distributed roughness parameters in a hydrodynamic model and estimated these parameters, using the observed WSE profiles along the stream as input. A case study was conducted in the Åmose stream, Denmark. The results showed that UAV-borne WSE can identify significant variations of the Manning–Strickler coefficients, along this small and highly vegetated stream and over time. Moreover, the model performed extremely well using distributed roughness coefficients, but it could not reproduce WSE satisfactorily using uniform roughness. We concluded that distributed roughness coefficients should be considered, especially for small vegetated rivers, to improve model performance, both locally and globally. Spatially distributed parameterizations of the effective channel roughness could be constrained with UAV-borne WSE. This study demonstrated for the first time that UAV-borne WSE can help to understand the variations of hydraulic roughness, and can support efficient river management and maintenance.

**Keywords:** UAV; altimetry; water surface elevation; hydrodynamic modeling; parameterization; regularization

## 1. Introduction

Water level, or water surface elevation (WSE) is the most elementary and important state variable among a number of quantities characterizing surface water systems [1]. Accurate and timely information about WSE is crucial for river and stream management and maintenance, flood risk assessment, preparedness, and mitigation strategies, especially in the context of extreme events and climate change. Traditional monitoring systems always suffer from lower spatial coverage, and the observations are inadequate to answer local questions. Discrete gauging data cannot resolve spatial

variations of fluvial variables (e.g., depth, surface slope, flood waves, etc.) and relevant hydrological and hydrodynamic processes between two gauging stations [2]. In many cases, farmlands or industrial parks are located where no gauging station is available. The lack of reliable WSE observations is a major concern to stakeholders. A precise estimate of WSE is needed. For instance, in Denmark, municipalities are legally required to guarantee that WSE remains below specified thresholds for given discharges (the so-called “kravkurve” or requirement curve), at given control stations. In order to achieve this goal, municipalities must monitor and maintain channel conveyance, especially during summer, when small Danish streams are heavily vegetated. However, this approach does not guarantee flood safety for farmland and infrastructure, throughout the entire river/stream reach but only at the control stations. Therefore, reach-scale reference WSE profiles for the given discharges are needed instead of requirement curves at a few locations, in the context of flood management. WSE is, thus, essential for flood management tasks, such as flood forecasting and flood risk mapping.

However, the current gauging network does not meet this demand. Hydrodynamic models can be used to interpolate spatial and temporal variations in the WSE between gauging stations. Integration of hydrodynamic models and observations has proved to be a powerful approach for augmenting our understanding of the process and is becoming increasingly important in streamflow forecasting, as demand for assessments of extreme climate events grows [3–9]. Nevertheless, a lack of spatially resolved observations can limit the skill of these models in terms of predicting WSE at a local scale.

Bathymetry and roughness are the most important factors influencing the prediction of inundation extent and water level in many hydrodynamic models [10–12]. Bathymetry can be measured or inferred but roughness is not directly measurable. The selection of roughness can be determined based on engineering judgement to provide physically plausible values. Another way is to calibrate roughness parameter using observations, e.g., inundation/WSE. The latter results in an effective roughness, which might be different from real physical roughness due to the uncertainties in model structure and bathymetry [12]. In addition, in most cases, one uniform roughness parameter is assigned/calibrated for the whole reach or floodplain [11]. Uniform effective parameters can also contribute to the equifinality phenomenon, i.e., several sets of effective roughness parameters perform equally well at evaluation locations. The reason is that roughness parameters compensate for errors in bathymetry, which might vary along the reach [13]. To better represent the behavior of a river, spatially distributed effective roughness should be used. The challenge here is to calibrate these distributed roughness parameters. To constrain such a high dimensional local model, high spatial resolution datasets, e.g., WSE are, needed [14]. The need for highly spatially-distributed WSE measurements was partially addressed by using satellite observations. Domeneghetti et al. [15] investigated the effect of Gauckler–Strickler coefficient on WSE simulation, by referencing to virtual stations at different reaches. Their study highlights the importance of spatial density of calibrating targets. Schneider et al. [16] obtained a more detailed parameterization of the Gauckler–Strickler coefficient of the Po river due to its densely distributed CryoSat-2 observations of WSE. A recent publication explored the capabilities of different satellite altimetry missions for calibrating both roughness and channel cross-section geometry [17]. Thanks to satellite radar altimetry, the value of introducing spatially varying roughness in hydrodynamic modeling has been highlighted. However, the spatial sampling interval of satellite altimetry is generally coarse (i.e., 80–315 km), except for the CryoSat-2 mission, which samples the Earth’s surface at an interval of 7.5 km at Equator. Nevertheless, a common shortcoming of satellite radar altimetry is the inability to deliver useful data for small rivers (< 100 m). Therefore, it is a challenge to deliver reliable, spatially resolved WSE datasets for small rivers [18].

Unmanned aerial vehicles/systems (UAV/UAS) have opened a new era to collect highly resolved spatial and temporal data sets for a variety of applications and end users [19,20]. In recent years, applications of UAV have grown rapidly in environmental monitoring and many different payloads have been explored, such as imaging and ranging devices (RGB, multispectral, hyperspectral, thermal, lidar, and radar sensors). Nevertheless, in many cases, UAV research has focused on land cover/change mapping, vegetation mapping, precision agriculture, crop growth monitoring, disaster mapping,

and soil erosion/characterization mapping [21]. UAV studies on river dynamics, especially streamflow monitoring, are still in early stages [2]. Currently, the integration of UAV imagery and optical velocimetry has enabled characterization of surface flows through appropriate techniques (e.g., Structure from Motion (SfM), Particle Image Velocimetry (PIV), Particle Tracking Velocimetry (PTV)) [21]. Recently, Bandini et al. [22] presented a new application of UAV, i.e., a UAV-borne radar altimeter, for WSE and water surface slope monitoring. In many ways, UAV-based radar altimetry has properties not unlike satellite altimetry, but with advantages at a small spatial scale and high ground resolution. Specifically, the radar footprint for low-altitude UAV flights is just a few decimeters in size, which allows observations of WSE in small streams; low-cost and flexible campaigns allow high spatial and temporal coverage. Moreover, UAV-based altimetry shows advantages over UAV-borne photogrammetry and lidar, in terms of accuracy and efficiency [23]. This approach can greatly advance the monitoring and modeling of small streams for both science and engineering practices.

Considering the above discussion on the demand of high spatial resolution WSE data and hydrodynamic model parameterization, the aim of this study was twofold. First, we apply a new approach proposed by [23] to collect a distributed WSE dataset of small streams. Second, we exploit the value of this dataset in terms of hydrodynamic modeling. Numerical experiments are undertaken to explore the effect of distributed/uniform roughness parameters on WSE simulation and to evaluate the effect of vegetation conditions on flood risk. Approaches and workflows are demonstrated for a case study focusing on a 2.3-km long reach of the Åmose river, Denmark. The findings will enrich current data collection methods and support the understanding of channel roughness effects and river management.

## 2. Materials and Methods

### 2.1. Study Area

The study area (Figure 1) was located east of the Tissø Lake in the Sjælland Region, Denmark. Here, Åmose å flows through a mixture of natural land, agriculture, and forests. Figure 2 shows the flow regime of Åmose å. The mean annual discharge was ca.  $0.78 \text{ m}^3/\text{s}$ , with large interannual (Figure 2a) as well as seasonal variations, i.e., high flow in the cold season and low flow usually in July–August (Figure 2b). The low flow shows a slight increase while the high flow is very similar to the long-term average in the recent decade (Figure 2c,d). Åmose å has recently been flooded in 2015 and 2016 (peak flow of  $5.30 \text{ m}^3/\text{s}$  and  $4.75 \text{ m}^3/\text{s}$ , respectively), which caused an inundation of farmland.

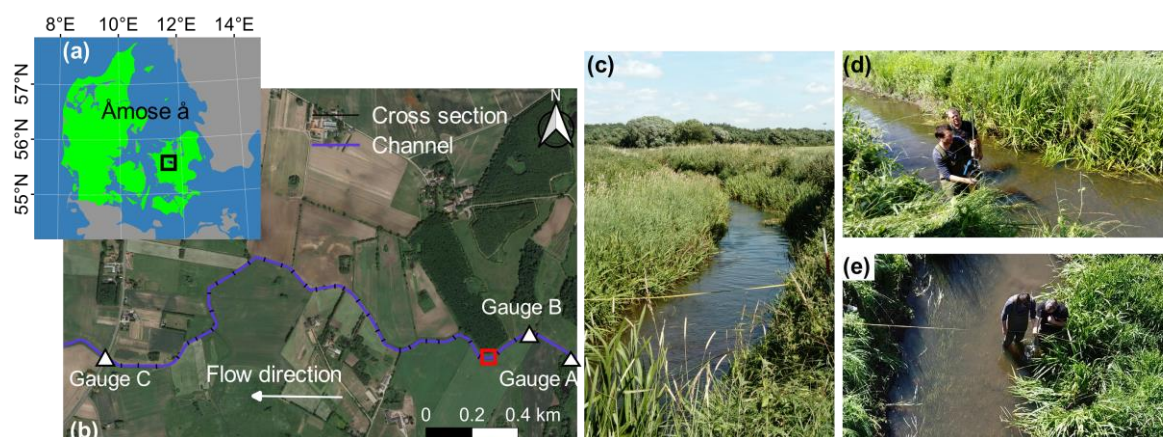


**Figure 1.** Field site and channel views. (a) Map showing the study area (Åmose å) in the western part of Zealand, Denmark. (b) The studied reach of Åmose å. (c) A photograph showing the upstream view. (d) A photograph showing the side view of the channel. (e) A photograph showing the top view of the channel. Photos were taken on 19 June 2018 at the site, indicated by red rectangle in (b).

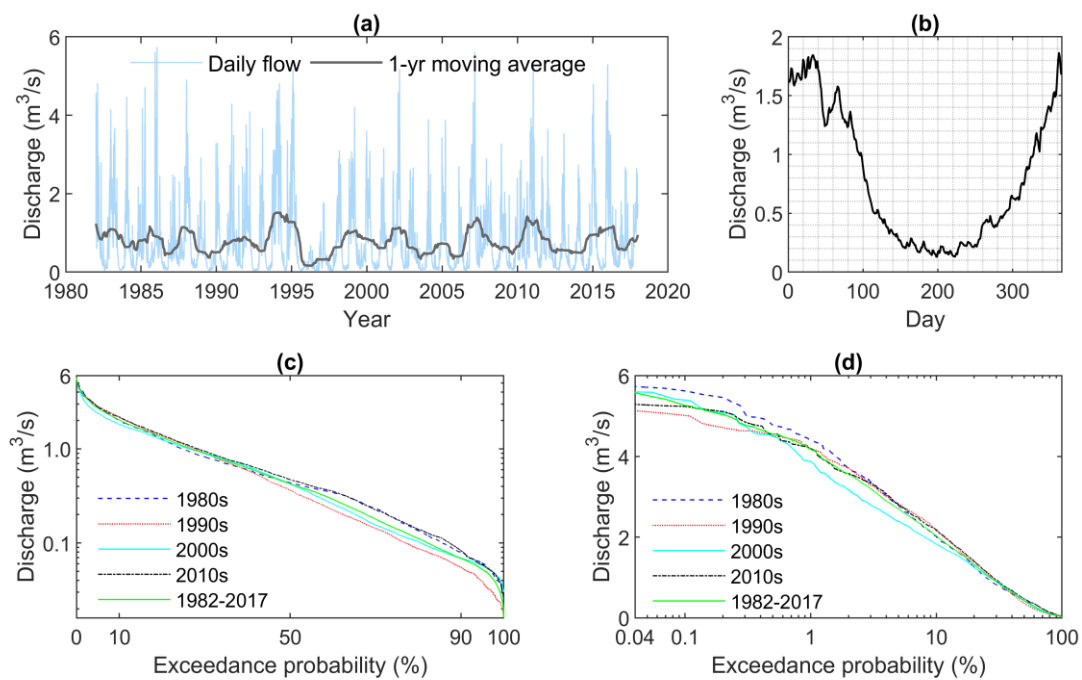


**Figure 2.** Flow regime of Åmose å. (a) Daily discharge during 1982–2017. (b) Multi-year averaged daily flow. (c) Flow duration curve with the low flow highlighted (discharge in logarithmic scale). (d) Flow duration curve with the high flow highlighted (exceedance probability in logarithmic scale).

We focused on a 2.3-km long reach of the Åmose stream, roughly between Kirke Eskilstrup and Ugerløse. The first 1.8 km reach was very narrow (1.4–2.0 m) (Figure 1c) and the last 0.5 km was a little wider (2.4–2.8 m). The average channel depth was ca. 2 m. The stream has mild slopes and an irregular longitudinal profile. Channel conveyance was highly influenced by summer vegetation (Figure 1c–e). Downstream from the studied reach, the stream continued to the west and discharged into the Tissø Lake.

## 2.2. Data Collection

UAV-borne WSE data were collected via a UAV altimetry system, which consisted of the platform, a radar sensor, and a Global Navigation Satellite System (GNSS). The radar ranging sensor mounted on the platform was the IWR 1443 model, with a center frequency of 77 GHz and 4 GHz continuous bandwidth. Thus, the range resolution was up to 4 cm. Similar to satellite altimetry, the GNSS measured the altitude of the UAV, while the radar sensor measured the range between the UAV and water surface. Therefore, the WSE could be calculated by subtracting the range from the UAV altitude. The technical details are described in Bandini et al. [22,23].

UAV field campaigns were conducted four times on 7 August, 5 September, 4 October, and 21 November of 2018. For each campaign, it took about half an hour of flight time to survey this 2.3-km reach. During the first survey, the whole reach was vegetated naturally. After this, the vegetation of the lower 0.5-km reach was cut on 11 August. No vegetation cuts were performed in September, and the second vegetation cut was conducted during 9 and 10 October, for the whole reach. Therefore, the channel conditions for the second and third campaigns should be similar.

Figure 3 shows the WSE variation and the changes of relative differences of WSE between three gauging stations, i.e., between gauge A and gauge B, and between gauge B and gauge C (Figure 1). Specifically, when vegetation downstream of gauge C was cut on 11 August (indicated by blue dash-dotted line), WSE of gauge C had decreased (blue line in Figure 3a), although that of gauge B and gauge C had increased, and the difference between gauge C and gauge B had increased sharply (red line in Figure 3b). Moreover, the hydrograph at gauge C did not resemble that at gauge B and gauge A,

after the vegetation cut on 11 August (hydrograph between two vertical lines). Similarly, vegetation cut in October also had a significant influence on the WSE of all three stations.

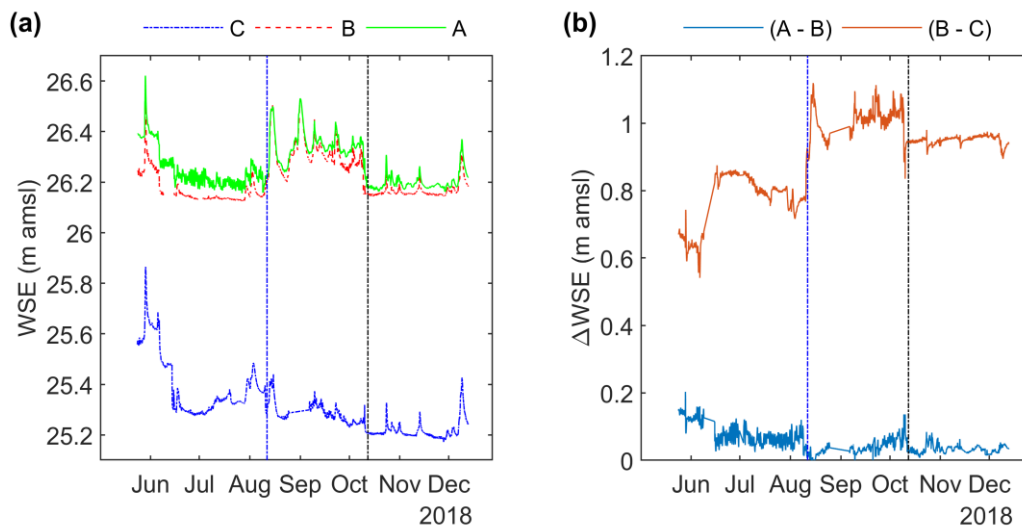


**Figure 3.** In-situ water surface elevation (a) from the three gauging stations, as shown in Figure 1, and the WSE differences (b) between the adjacent stations. The blue and black dash dot lines indicate the dates of vegetation cutting activities. Note that, gauges A, B, and C are located from upstream to downstream, as indicated in Figure 1.

As explained in [23], in-situ observations of WSE were obtained with levelling and the real time kinematic (RTK) GNSS technique. Along the surveyed reach, metal poles were installed in order to have stable in-situ reference points. The horizontal coordinates and the elevation above mean sea level (amsl) of these poles were measured on multiple days with an RTK GNSS rover station, to evaluate the stability of the poles and to average out the GNSS measurement errors. The height offset ( $\Delta z$ ) between each metal pole and the closest water surface point was measured with a levelling instrument. By subtracting  $\Delta z$  from the pole elevation, in-situ WSE observations were obtained with an accuracy of ca. 2–3 cm.

Discharge measurements (at gauge A and gauge B, refer to Figure 1) were retrieved with the instrument OTT MF Pro (OTT HydroMet, Germany). The instrument has a build-in pressure transducer to measure water depth and a velocity sensor, based on electromagnetic induction. Velocity was generally measured at 3 different depths and at least 9 different intervals, across the river width. The mid-section method was applied to estimate discharge from water depth and velocity observations (ISO 748:2007). The discharge estimates were, thus, directly obtained from the velocity measurements distributed throughout the flow cross-section. No rating curve or roughness coefficient was used in the estimation.

### 2.3. Data Processing

The radar provides full waveform datasets, thus, the return representative of the water surface had to be identified during post-processing. First, a river mask was created to remove observations retrieved at flight locations that were above land or other non-river objects. Specifically, the mask was generated by buffering the river centerline by 1.5 m on each side. The buffer zone was chosen according to the stream size to approximate the river mask. Second, the peak return of each waveform was extracted inside the waveform window (generally 10 m wide) where the water surface was expected to be found. Finally, outliers were removed by investigating the return power, i.e., targets which showed a power return below the threshold value were not expected to be water and were discarded. Moreover, for comparison with the hydrodynamic model outputs, we further processed the remaining data to a

lower spatial resolution, i.e., 3 m, by averaging the observations within a 3-m interval. Details of the data processing workflows can be found in Bandini et al. [23].

#### 2.4. River Model Setup

The general configuration of the study reach is shown in Figure 1b. The channel geometry is described by means of 32 cross-sections, which were surveyed at an interval of around 70 m, using a RTK GNSS rover. For each cross-section, the elevations of the banks and river bottom were measured at an interval of around 0.5 m, to capture the variable topography.

MIKE Hydro River was used to simulate cross-section averaged flow. MIKE Hydro River used a one-dimensional (1D) simulation engine, which solved the fully dynamic De Saint Venant equations using an implicit 6-point finite-difference scheme [24]. The model was forced with observed discharge from the upstream end, and the downstream boundary condition was defined by a rating curve (i.e., Q/h relation in the software). The rating curve was computed using Gauckler–Manning–Strickler formula that expresses discharge as a function of cross-section geometry, channel bed slope and roughness coefficient. Note that uniform flow was assumed, i.e., energy slope was approximated by bed slope. The roughness coefficient was represented by the Gauckler–Strickler coefficient  $K_s$  (the symbol M is used in MIKE Hydro River;  $K_s = 1/n$ , n being the Manning coefficient).

Four model configurations were set separately for 7 August, 5 September, 4 October, and 21 November of 2018. The observed discharge was 25.6 l/s, 72 l/s, 60 l/s, and 71.5 l/s for the four configurations, respectively. The simulation time for the steady state was 1 day, with a time step of 30 s.

#### 2.5. Calibration

The model calibration process focused on the estimation of the optimal values of coefficient  $K_s$ , which is varying between the cross sections. Therefore, in total, 32 parameters were to be calibrated. Here, we used a non-linear least-squares solver with a computationally efficient algorithm, i.e., Levenberg–Marquardt. Considering the large number of parameters, we applied the optimization with regularization to stabilize the inverse problem. The intuitive motivation for regularization was that the neighboring parameters should not have large variations, over a short distance [25]. Smoothness was often enforced by penalizing the discontinuities between neighboring parameters [26]. Therefore, the objective function consisted of the residuals of simulated and observed WSE and a regularization term that penalized abrupt changes of the Gauckler–Strickler coefficients, between the neighboring cross-sections, as used in [16,17]:

$$obj = \left\{ \sum_{i=1}^{N_{WSE}} (H_{s,i} - H_{o,i})^2 + \lambda \sum_{j=1}^{N_{XS}-1} (K_{s,j+1} - K_{o,j})^2 \right\}$$

where  $K_s$  is the Gauckler–Strickler coefficient to be calibrated;  $H_s$  and  $H_o$  are the simulated and observed WSE, respectively;  $N_{WSE}$  and  $N_{XS}$  are the total number of UAV-borne WSE observations and cross-sections; and  $\lambda$  is a regularization parameter (penalty) used to regularize the degree of smoothness.

To determine the regularization parameter  $\lambda$ , the  $\ell$ -curve approach [27] is used. The  $\ell$ -curve approach aims to strike a balance between data misfit and some property that measures extravagant behaviors. Therefore, a value of  $\lambda_\ell$  was chosen in order to keep both below the appropriate upper bounds. In most cases, the plot of data misfit and model smoothness showed an “ $\ell$ ” form. The  $\lambda$  value at the corner of the “ $\ell$ ” was taken as  $\lambda_\ell$ . Note that, in real world inverse problems, the “ $\ell$ ” form might not be as distinct. In this study, we represent model misfit by root-mean-square-error of the simulated WSE and observed WSE. Similarly, model smoothness was indicated by root-mean-square deviation of adjacent  $K_s$ . An example showing the effect of penalty  $\lambda$  on model performance and roughness coefficients is depicted in Figure 4. As shown in Figure 4a, without penalty, i.e.,  $\lambda = 0$ ,  $K_s$  is very diverse and discontinuous. As  $\lambda$  increases,  $K_s$  gets gradually smoother. Figure 4c shows the “ $\ell$ ” form and the

'best'  $\lambda_\ell$  is found in the corner. The value of  $\lambda_\ell$  was set as 0.04, 0.03, 0.04, 0.02 for August, September, October, and November, respectively, in posterior analyses.

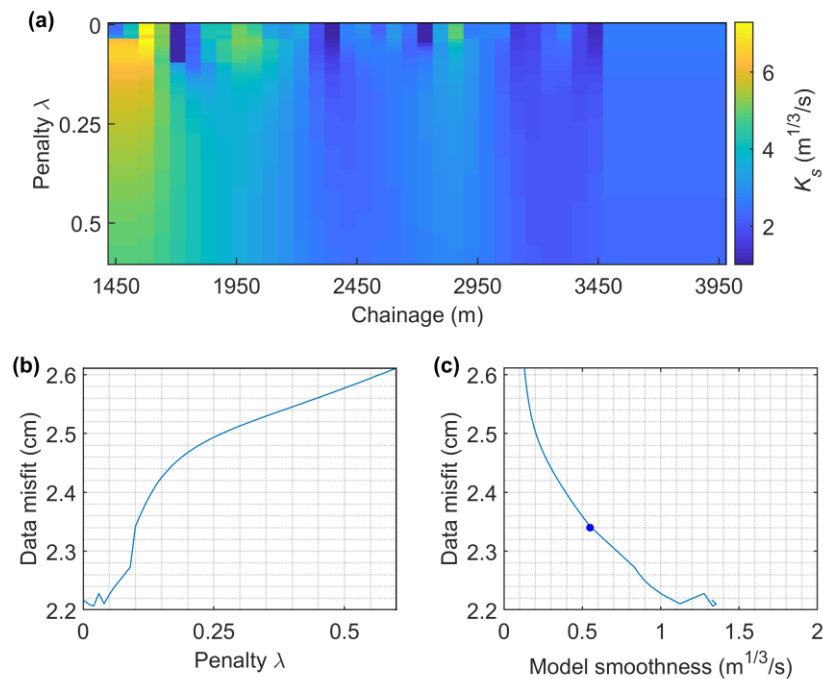


**Figure 4.** Exemplary sensitivity of parameter  $K_s$  smoothness (a) and model performance (b) of the regularization parameter (i.e., penalty  $\lambda$ ). The  $\ell$ -curve (c) is shown for the trade-off between data misfit and model smoothness. Note that, the blue dot indicates the 'best'  $\lambda_\ell$  used for further calibration.

### 3. Results

#### 3.1. UAV-Borne WSE

As shown in Figure 5, UAV altimetry can deliver a very high-resolution WSE dataset. The water surface slope is clearly shown, which was not possible using sparse traditional gauging networks. UAV-borne WSE matches in-situ measurement very well (RMSE < 3 cm). There was no significant difference of data accuracy between the four scenarios, although the vegetation conditions were noticeably different. Clearly, the longitudinal profiles illustrated the influence of the vegetation condition on WSE. After the first vegetation cutting of the downstream part, the longitudinal profiles of September and October obviously differed from that of August. It was clear that downstream of chainage of 3000 m, WSE had sharply dropped due to a lower channel roughness. It should be noted that the seasonal variability of the roughness could raise or lower WSE [13], but such seasonal effects were expected to be uniform along the whole reach and would not affect upstream and downstream differently, as was evident in our dataset.

Moreover, discharge in September and November was almost equal, but WSE in November was much lower than that in September (Figure 5). This demonstrated the important effect of vegetation on WSE. The second vegetation cutting (for the whole reach) was conducted after the October WSE campaign. Therefore, the spatial patterns of channel roughness were similar in August and November, and the longitudinal WSE profiles were also similar (Figure 5). Furthermore, although the discharge in November was almost three times higher than the discharge in August, WSE was nearly the same in November and August, which again confirmed the role vegetation plays in controlling WSE. It should be noted that, the downstream area was cleaned twice, and therefore, the WSE difference between October and November was not as large in the downstream region as in the upstream region.

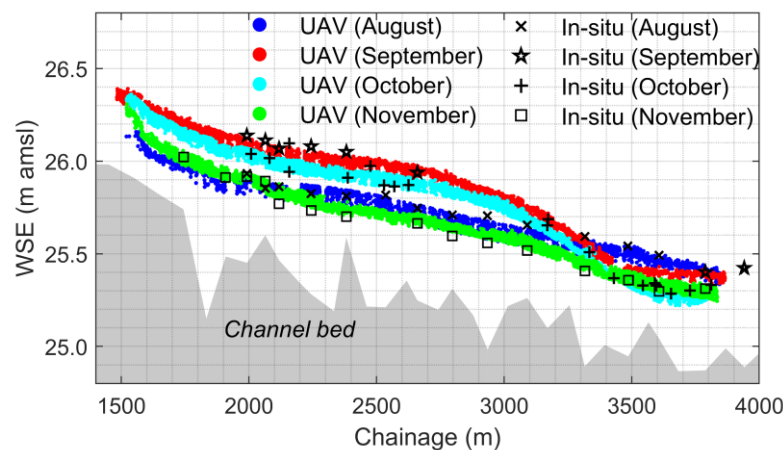


**Figure 5.** Longitudinal profile plots of WSE derived from four UAV campaigns against in-situ measurements. The shaded area indicates the channel bed, which is represented by the deepest point in each cross-section.

### 3.2. Calibration of a Hydrodynamic Model

#### 3.2.1. Sensitivity Analysis of Gauckler–Strickler $K_s$

Sensitivity of the spatially uniform Gauckler–Strickler coefficients on model performance was evaluated based on root mean square error (RMSE) of the simulated and UAV-borne WSE. The model was run using a range of values of Gauckler–Strickler  $K_s$ . As shown in Figure 6, the model performance was very sensitive (RMSE ranging from a few cm to a few dm) to Gauckler–Strickler  $K_s$ , which indicated that the selection of  $K_s$  value was a determinant factor to reproduce WSE accurately.

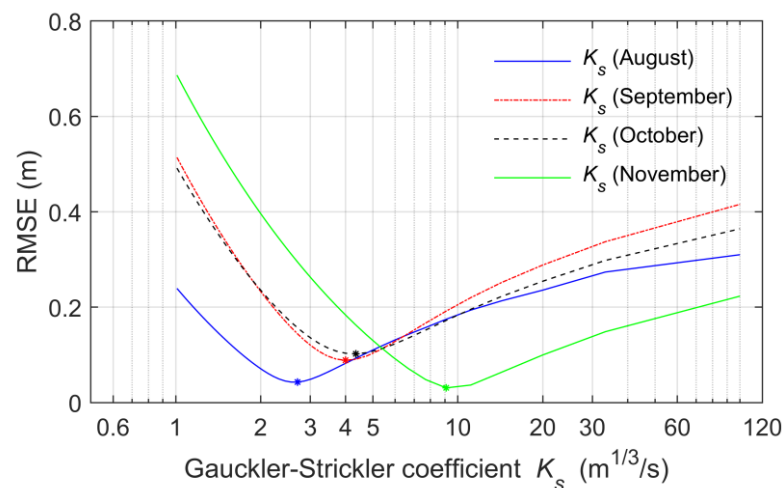


**Figure 6.** Model performance for different calibration setups as a function of spatially uniform Gauckler–Strickler  $K_s$ . Asterisks indicate the optimum values for different setups.

We could also see that temporal variation of  $K_s$  was remarkable during the four-month period. The optimal  $K_s$  value for August, September, October, and November were  $2.7 \text{ m}^{1/3}/\text{s}$ ,  $4.0 \text{ m}^{1/3}/\text{s}$ ,  $4.4 \text{ m}^{1/3}/\text{s}$ , and  $9.1 \text{ m}^{1/3}/\text{s}$ , respectively (Figure 6). We are aware that the roughness coefficient varies with discharge. More specifically, roughness coefficients decreases with increasing discharge to some point, showing an asymptotical behavior [13,28]. However, the discharges observed during the four campaign dates were similar, especially those of September (72 l/s), October (60 l/s), and November (71.5 l/s). The variation of the roughness coefficient could, therefore, primarily be explained by the vegetation condition. In August, the whole reach was highly vegetated, which resulted in a higher

flow resistance, i.e., smaller Gauckler–Strickler  $K_s$ . For September and October, vegetation in the downstream region was cut, which led to a larger  $K_s$ . The small difference of  $K_s$  could be attributed to the slight underestimation of WSE (Figure 5). Further, in November, vegetation of the whole reach was cut. Therefore, the roughness decreased significantly.

### 3.2.2. Spatio-Temporal Variation of the Gauckler–Strickler $K_s$

All four real case scenarios showed spatial variability of the Gauckler–Strickler  $K_s$  (Figure 7). For the upstream 1.8-km reach, the variation in the Gauckler–Strickler  $K_s$  was relatively small and the variation was generally consistent from August to October, especially during the September–October period (Figure 7b). On the contrary, for the downstream 0.5-km reach, the differences were pronounced. In August,  $K_s$  of the downstream region was very close to that of the upstream region. However, in September,  $K_s$  of the downstream region had increased significantly. This could be explained by the vegetation cut on 11 August 2018. Short in-channel grass had much smaller resistance, i.e., higher Gauckler–Strickler  $K_s$ . The difference of  $K_s$  in August and September clearly demonstrated the influence of vegetation on roughness coefficient. Moreover, the sharp drop in WSE was clearly captured by the UAV observations, as shown in Figure 5. Given that there was no vegetation cutting between the WSE campaigns in September and October, the spatial variability of  $K_s$  was very similar, especially for the upstream 1.8-km reach (Figure 7b). This was also revealed by the similar pattern of UAV observations of WSE (Figure 5). However,  $K_s$  of the downstream region exhibited small differences between September and October. This could probably be attributed to vegetation growth and the measurement error of the WSE observations of the October campaign. As shown in Figure 5, the observations in the downstream region in October were slightly lower than in-situ observations. Comparatively,  $K_s$  in November was larger than other cases, in general, which could be explained by vegetation cutting of the whole reach.

Regarding the August case, calibrated  $K_s$  varied from 1.3 to 6.5  $\text{m}^{1/3}/\text{s}$ , which was much smaller than the values usually used in the hydrodynamic modeling of large rivers [16,29,30]. However, this studied channel was extremely narrow (~2 m), flat (~30 cm/km), and highly vegetated. As shown in Figure 1, reeds along the channel banks and in-channel submerged weeds acted as an obstruction to flow, increasing the hydraulic resistance. As Chow [31] reported, submerged plants can cause a multiplication up to 20, compared to the non-vegetated channels. Therefore, this higher roughness was reasonable. Similar values were reported in De Doncker et al. [32] for an even wider channel (ca. 10 m).

In November,  $K_s$  increased along the entire reach because aquatic vegetation was cut throughout.  $K_s$  ranged from 4.4 to 14.3  $\text{m}^{1/3}/\text{s}$ . As expected, the magnitude of  $K_s$  changed but the spatial pattern generally remained comparable to that in August, especially for the first 1.8-km of the reach. However, the evolution in the downstream region was surprising, given that it was cleaned after the October campaign— $K_s$  of the last 0.5-km of the reach in November should have been larger than that in October. As mentioned before, the WSE of the downstream region in the October campaign was slightly underestimated, which resulted in a smaller roughness coefficient, i.e., a larger Gauckler–Strickler  $K_s$ .

Our results clearly showed the effect of vegetation on stream conveyance. The extent to which vegetation affected roughness depended on many factors, such as flow depth, flow velocity, submerged vegetation density, vegetation geometry, etc. [33]. For a given vegetated river, seasonal phenology could be a key control on flow resistance, as demonstrated by Shih and Rahi [34], who reported that the roughness coefficient tripled over a six-month period.

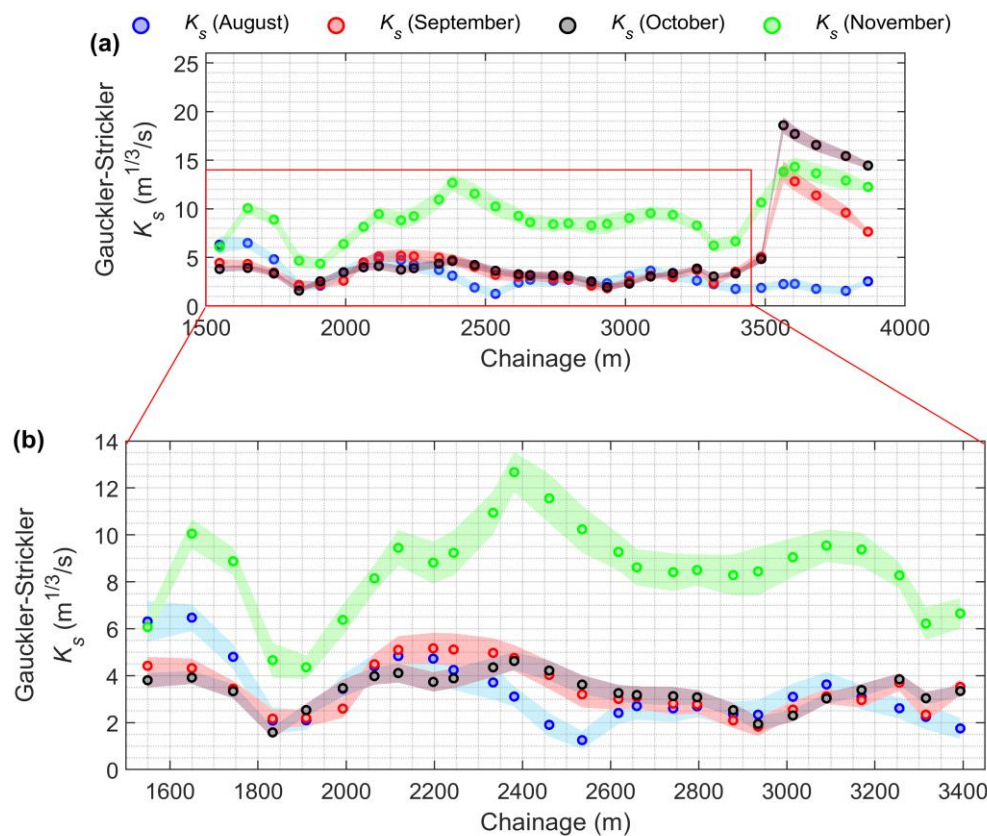


**Figure 7.** Variation of the Gauckler–Strickler coefficient  $K_s$  of four months, i.e., August, September, October, and November. The shaded area indicates a 95% confidence interval. (b) zoom-in of (a) focusing on the first 2-km reach.

### 3.2.3. Comparison of Model Performance using Distributed and Uniform Gauckler–Strickler $K_s$

Figure 8 shows the model simulations using both distributed and uniform Gauckler–Strickler  $K_s$ . Clearly, models using the distributed  $K_s$  significantly outperformed their counterparts, even if the latter used calibrated optimal values (i.e., obtained through sensitivity analysis in Section 3.2.1). Using the distributed values, the models could reproduce WSE with a very high accuracy (RMSE < 2.0 cm). Comparatively, although the models could reproduce WSE to some degree using uniform roughness, model performances were much worse (in terms of RMSE, shown in Figure 8). The difference of model performance became much more pronounced in September and October (1.3 cm vs. 8.9 cm, 1.1 cm vs. 10.2 cm). For these periods, large differences between the upstream and downstream region were expected because aquatic vegetation was only cut in the downstream region. Figure 8b,c clearly reveal that the shape of the water surface elevation profile could not be satisfactorily reproduced using a uniform roughness coefficient in the hydrodynamic model. It is important to note that we would not be able to predict water level with a ~2 cm accuracy. Obviously, the calibrated effective roughness coefficients compensate for the errors in the discharge measurements and the errors in the bathymetry, which would have an impact on predictive performance in a new situation. There is a tradeoff between model misfit and model smoothness in model calibration, which we need to pay attention to, in order to get a compromise solution, as mentioned in Section 2.5.

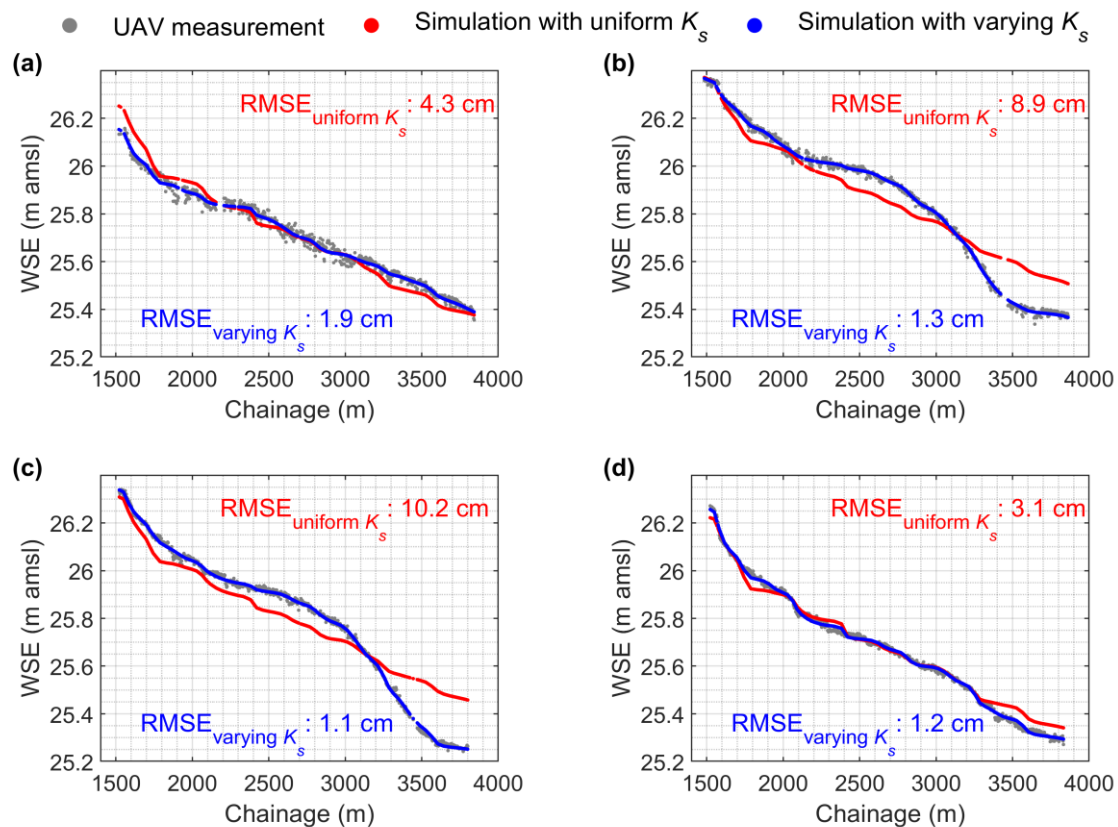


**Figure 8.** Simulated WSE against UAV-borne measurements using spatially uniform and distributed Gauckler-Strickler  $K_s$  (a) August, (b) September, (c) October, and (d) November.

#### 4. Discussion

This study showcased an application of UAV-borne WSE for hydrodynamic model parameterization. With highly spatially resolved WSE, a model with distributed roughness parameters could be calibrated and was shown to provide more accurate simulations of WSE. The shortcomings of uniform roughness have been pointed out by, e.g., Pappenberger et al. [35]. In many cases and over a range of scales, model performance is insufficient when using globally uniform roughness coefficient, and this is particularly important in flood-risk assessment [36]. As shown in Figure 8, models failed to reproduce local phenomena in the downstream region, especially for September (Figure 8b) and October (Figure 8c). Figure 8 proves that using distributed roughness parameters is a good solution to reproduce local phenomena. As channel roughness is affected by many factors, such as grain size of the bed material, vegetation height and density, channel sinuosity, channel obstructions, one single effective value of the roughness has to compensate for all factors. Therefore, a model with uniform roughness is unlikely to predict WSE everywhere along the reach. On the other hand, it should be noted that calibrated roughness parameters might differ from those obtained using engineering judgement (subjective and extensive), but it is more important to accurately predict WSE rather than roughness [11]. However, in our case, the calibrated roughness parameters are reasonable compared to other studies [32,34,37]. With high-resolution spatially distributed UAV-borne WSE, we are able to move forward into a “new normal” in hydrodynamic modeling. We are aware of the issue of computation time for the calibration of highly parameterized models. In this study, calibration of spatially distributed parameters takes around 30 times longer than that of the calibration of uniform parameters, using the Levenberg–Marquardt algorithm. This was mainly due to the computation of Jacobian matrix in the optimization. However, a more efficient algorithm and cloud computing would expedite model optimization. Therefore, calibration of the distributed effective roughness parameters is recommended.

It is well-known that roughness varies with discharge and, thus, changes in time. Therefore, in addition to spatial variation, roughness coefficients also vary in time, both seasonally because of vegetation growth/decay, and over short time-scales because of discharge variability. Therefore, a constant uniform coefficient might not be appropriate to simulate water level and discharge. To improve model simulations, spatially-distributed WSE over a sufficient time period is needed. Future work could target the calibration of temporally-varying spatially-distributed roughness coefficients for rivers and streams. To this end, time-lapse UAV altimetry datasets with a high spatial resolution should be combined with point gauging station datasets with a high temporal resolution.

One might argue that a parsimonious model should be preferred over a highly parameterized model. The regularization terms in the calibration objective function suppress the spatial variation of the roughness parameters, unless such variations are necessary to achieve an acceptable data fit. Thus, implicitly, the regularization ensures that the calibrated model is parsimonious. In a real-world scenario, we do not know a priori how the roughness parameters vary in space and the hydraulic inversion approach presented here is a way to map such variations. In this context, it is important to note that we only learned about the schedule of vegetation cutting operations in the investigated stream reach after the hydraulic inversion, and it turned out that the hydraulic inversion correctly identified the real cutting operations, as shown in Figure 8.

Spatial variation of vegetation conditions and roughness could be much more significant for longer river reaches, and the effect of spatially-distributed roughness on model simulations could be even more important. UAV altimetry offers a cost-effective option to survey WSE along 10 s or even 100 s of river-kilometers at high accuracy and spatial resolution. Depending on site conditions, a trained operator can cover ca. 10 river kilometers per day, using a single drone and radar altimetry payload. Survey efficiency can be significantly increased, if flights can be conducted beyond the visual line of sight (BVLOS). Moreover, the radar altimetry payload is relatively inexpensive, and several UAV platforms can be combined to cover longer river reaches. The most important operational challenges we have encountered in UAV radar altimetry survey are (i) accurate navigation of the drone platform over the river centerline (this is especially important for narrow rivers) and (ii) accurate drone altitude from post-processed GNSS records, which often requires a local GNSS base station next to survey locations.

High-resolution UAV altimetry WSE datasets combined with hydrodynamic simulation models can provide valuable tools for river maintenance and flood-risk management. As mentioned in the introduction, requirement curve prescribes WSE variation at specific control stations, while WSE between the two control stations is not constrained at all. As illustrated in Figure 9, for a given discharge  $q$ , WSE should be below the requirement curve (Figure 9a). However, at other locations (see red rectangle in Figure 9b), WSE could go beyond the warning level due to the low channel conveyance induced by growth of vegetation, blockage by fallen trees, etc. By establishing a reference WSE profile, it is straightforward to monitor and maintain stream conveyance and flood risk anywhere along the stream. One might argue that this problem could also be solved by establishing more control stations. However, establishment and maintenance of many control stations is impractical and could be prohibitively expensive. On the contrary, reach scale WSE profile can be obtained cost-effectively using a hydraulic river model. However, hydraulic models need to be calibrated and calibration requires spatially distributed WSE datasets. The UAV-derived distributed WSE dataset as presented in previous sections is extremely valuable for parameterization and validation of such river models.

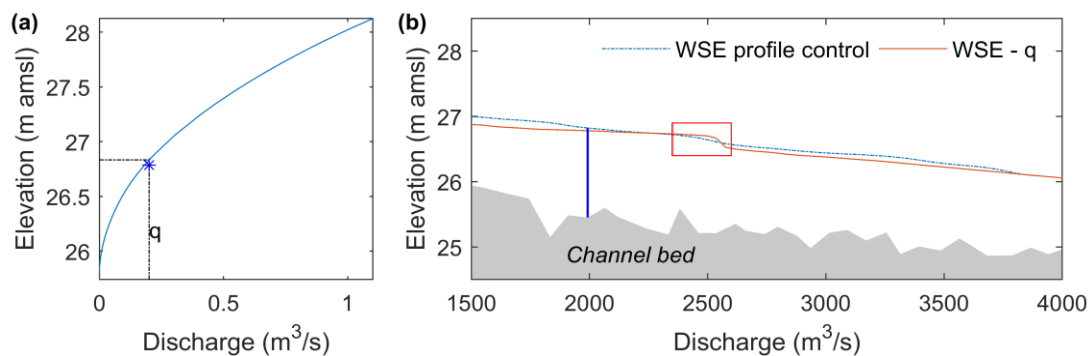


**Figure 9.** Illustration of curve control and profile control. (a) Requirement curve at one control station. (b) Reach-scale WSE profile control (dash-dot) and a synthetic WSE profile for a given discharge, e.g.,  $q$  in (a). The blue bar indicates the location of the control station shown in (a). Red rectangle highlights the position where the WSE does not meet the requirement WSE profile.

## 5. Summary and Conclusions

This work presents a new application of UAV for monitoring water surface elevation (WSE). UAV altimetry is more cost-effective, time-saving, and flexible, compared to traditional field survey. We showcased this approach by collecting spatially distributed WSE for a small stream, i.e., Åmose å in Denmark. Four field campaigns were conducted over a 2.3-km reach. The results were very promising, i.e., UAV altimetry could deliver very high resolution (ca. 0.5 m) and accurate (ca. 3 cm) distributed observations of WSE.

Further, we demonstrated the value of such a high-resolution dataset via the calibration of a hydrodynamic model. Determination of roughness coefficients has often been based on subjective expert judgement in engineering applications but has a dominant influence on WSE predicted by hydrodynamic simulators. As argued by Werner [38], literature values might not always be appropriate due to the different conditions in the field. On the other hand, hydrodynamic models which use a uniform roughness coefficient are unable to reproduce the local phenomena [35]. In this study, we introduced distributed roughness coefficients in the hydrodynamic model, to accurately reproduce the observed water surface elevation profiles.

The results showed that UAV-altimetry derived WSE was able to constrain spatially distributed roughness parameters. Moreover, we found that using distributed roughness coefficients, models could reproduce WSE with a very high accuracy ( $< 2$  cm), without losing local phenomena. Comparatively, the commonly used approach, i.e., uniform roughness for entire reaches, could not reproduce WSE at many locations, even though the overall performance was acceptable to some degree. Performance of the uniform-roughness models degraded when the degree of channel heterogeneity increased. Therefore, spatially distributed roughness coefficients should be introduced to capture the local phenomena, which is especially important in terms of flood-risk assessment.

In the context of Danish stream management, instead of requirement curves at certain control stations, we recommend adopting WSE profile as a requirement control that can be established using a hydrodynamic model and UAV altimetry. This approach is applicable to other streams worldwide.

**Author Contributions:** Conceptualization, L.J. and P.B.-G.; methodology, L.J. and P.B.-G.; software execution, L.J.; data curation, F.B., O.S. and I.K.J.; writing—original draft preparation, L.J.; writing—review and editing, L.J., P.B.-G., F.B., O.S., and I.K.J.; visualization, L.J.; supervision, P.B.-G.; project administration, P.B.-G.; funding acquisition, P.B.-G. All authors have read and agreed to the published version of the manuscript.

**Funding:** The Innovation Fund Denmark is acknowledged for providing funding for this study via the project RIVERSCAPES (7048-00001B).

**Conflicts of Interest:** The authors declare no conflict of interest.

## References

1. Blöschl, G.; Gaál, L.; Hall, J.; Kiss, A.; Komma, J.; Nester, T.; Parajka, J.; Perdigão, R.A.P.; Plavcová, L.; Rogger, M.; et al. Increasing river floods: Fiction or reality? *Wiley Interdiscip. Rev. Water* **2015**, *2*, 329–344. [[CrossRef](#)] [[PubMed](#)]
2. Tauro, F.; Selker, J.; van de Giesen, N.; Abrate, T.; Uijlenhoet, R.; Porfiri, M.; Manfreda, S.; Caylor, K.; Moramarco, T.; Benveniste, J.; et al. Measurements and Observations in the XXI century (MOXXI): Innovation and multi-disciplinarity to sense the hydrological cycle. *Hydrol. Sci. J.* **2018**, *63*, 169–196. [[CrossRef](#)]
3. Bauer-Gottwein, P.; Jensen, I.H.; Guzinski, R.; Bredtoft, G.K.T.; Hansen, S.; Michailovsky, C.I. Operational river discharge forecasting in poorly gauged basins: The Kavango River basin case study. *Hydrol. Earth Syst. Sci.* **2015**, *19*, 1469–1485. [[CrossRef](#)]
4. Chang, C.-H.; Lee, H.; Hossain, F.; Basnayake, S.; Jayasinghe, S.; Chishtie, F.; Saah, D.; Yu, H.; Sothea, K.; Du Bui, D. A model-aided satellite-altimetry-based flood forecasting system for the Mekong River. *Environ. Model. Softw.* **2019**, *112*, 112–127. [[CrossRef](#)]
5. Crochemore, L.; Ramos, M.H.; Pappenberger, F.; Perrin, C. Seasonal streamflow forecasting by conditioning climatology with precipitation indices. *Hydrol. Earth Syst. Sci.* **2017**, *21*, 1573–1591. [[CrossRef](#)]
6. Grimaldi, S.; Li, Y.; Pauwels, V.R.N.; Walker, J.P. Remote Sensing-Derived Water Extent and Level to Constrain Hydraulic Flood Forecasting Models: Opportunities and Challenges. *Surv. Geophys.* **2016**, *37*, 977–1034. [[CrossRef](#)]
7. Michailovsky, C.I.; Bauer-Gottwein, P. Operational reservoir inflow forecasting with radar altimetry: The Zambezi case study. *Hydrol. Earth Syst. Sci.* **2014**, *18*, 997–1007. [[CrossRef](#)]
8. Neal, J.; Schumann, G.; Bates, P. A subgrid channel model for simulating river hydraulics and floodplain inundation over large and data sparse areas. *Water Resour. Res.* **2012**, *48*, 1–16. [[CrossRef](#)]
9. Paiva, R.C.D.; Collischonn, W.; Bonnet, M.-P.; de Gonçalves, L.G.G.; Calmant, S.; Getirana, A.; Santos da Silva, J. Assimilating in situ and radar altimetry data into a large-scale hydrologic-hydrodynamic model for streamflow forecast in the Amazon. *Hydrol. Earth Syst. Sci.* **2013**, *10*, 2879–2925. [[CrossRef](#)]
10. Bates, P.D.; Pappenberger, F.; Romanowicz, R.J. Uncertainty in Flood Inundation Modelling. In *Applied Uncertainty Analysis for Flood Risk Management*; Imperial College Press: London, UK, 2014; pp. 232–269. ISBN 978-1-78326-312-7.
11. Di Baldassarre, G.; Schumann, G.; Bates, P.D.; Freer, J.E.; Beven, K.J. Flood-plain mapping: A critical discussion of deterministic and probabilistic approaches. *Hydrol. Sci. J.* **2010**, *55*, 364–376. [[CrossRef](#)]
12. Pappenberger, F.; Beven, K.; Horritt, M.; Blazkova, S. Uncertainty in the calibration of effective roughness parameters in HEC-RAS using inundation and downstream level observations. *J. Hydrol.* **2005**, *302*, 46–69. [[CrossRef](#)]
13. Domeneghetti, A.; Castellarin, A.; Brath, A. Assessing rating-curve uncertainty and its effects on hydraulic model calibration. *Hydrol. Earth Syst. Sci.* **2012**, *16*, 1191–1202. [[CrossRef](#)]
14. Fleischmann, A.; Paiva, R.; Collischonn, W. Can regional to continental river hydrodynamic models be locally relevant? A cross-scale comparison. *J. Hydrol. X* **2019**, *3*, 100027. [[CrossRef](#)]
15. Domeneghetti, A.; Tarpanelli, A.; Brocca, L.; Barbeta, S.; Moramarco, T.; Castellarin, A.; Brath, A. The use of remote sensing-derived water surface data for hydraulic model calibration. *Remote Sens. Environ.* **2014**, *149*, 130–141. [[CrossRef](#)]
16. Schneider, R.; Tarpanelli, A.; Nielsen, K.; Madsen, H.; Bauer-Gottwein, P. Evaluation of multi-mode CryoSat-2 altimetry data over the Po River against in situ data and a hydrodynamic model. *Adv. Water Resour.* **2018**, *112*, 17–26. [[CrossRef](#)]
17. Jiang, L.; Madsen, H.; Bauer-Gottwein, P. Simultaneous calibration of multiple hydrodynamic model parameters using satellite altimetry observations of water surface elevation in the Songhua River. *Remote Sens. Environ.* **2019**, *225*, 229–247. [[CrossRef](#)]
18. Jiang, L.; Nielsen, K.; Dinardo, S.; Andersen, O.B.; Bauer-Gottwein, P. Evaluation of Sentinel-3 SRAL SAR altimetry over Chinese rivers. *Remote Sens. Environ.* **2020**, *237*, 111546. [[CrossRef](#)]
19. Anderson, K.; Gaston, K.J. Lightweight unmanned aerial vehicles will revolutionize spatial ecology. *Front. Ecol. Environ.* **2013**, *11*, 138–146. [[CrossRef](#)]

20. McCabe, M.F.; Rodell, M.; Alsdorf, D.E.; Miralles, D.G.; Uijlenhoet, R.; Wagner, W.; Lucieer, A.; Houborg, R.; Verhoest, N.E.C.; Franz, T.E.; et al. The Future of Earth Observation in Hydrology. *Hydrol. Earth Syst. Sci.* **2017**, *21*, 3879–3914. [[CrossRef](#)]
21. Manfreda, S.; McCabe, M.; Miller, P.; Lucas, R.; Pajuelo Madrigal, V.; Mallinis, G.; Ben Dor, E.; Helman, D.; Estes, L.; Ciruolo, G.; et al. On the Use of Unmanned Aerial Systems for Environmental Monitoring. *Remote Sens.* **2018**, *10*, 641. [[CrossRef](#)]
22. Bandini, F.; Jakobsen, J.; Olesen, D.; Reyna-Gutierrez, J.A.; Bauer-Gottwein, P. Measuring water level in rivers and lakes from lightweight Unmanned Aerial Vehicles. *J. Hydrol.* **2017**, *548*, 237–250. [[CrossRef](#)]
23. Bandini, F.; Sunding, T.P.; Linde, J.; Smith, O.; Jensen, I.K.; Köppl, C.J.; Butts, M.; Bauer-Gottwein, P. Unmanned Aerial System (UAS) observations of water surface elevation in a small stream: Comparison of radar altimetry, LIDAR and photogrammetry techniques. *Remote Sens. Environ.* **2020**, *237*, 111487. [[CrossRef](#)]
24. DHI. *MIKE HYDRO River—User Guide*; DHI: Copenhagen, Danish, 2017.
25. Schmidt, M. Least squares optimization with L1-norm regularization. *CS542B Proj. Rep.* **2005**, *504*, 195–221.
26. Ke, Q.; Kanade, T. Robust  $L_1$  Norm Factorization in the Presence of Outliers and Missing Data by Alternative Convex Programming. In Proceedings of the 2005 IEEE Computer Society Conference on Computer Vision and Pattern Recognition (CVPR'05), San Diego, CA, USA, 20–25 June 2005; Volume 1, pp. 739–746.
27. Hansen, P.C.; O’Leary, D.P. The Use of the L-Curve in the Regularization of Discrete Ill-Posed Problems. *SIAM J. Sci. Comput.* **1993**, *14*, 1487–1503. [[CrossRef](#)]
28. Moramarco, T.; Singh, V.P. Formulation of the entropy parameter based on hydraulic and geometric characteristics of river cross sections. *J. Hydrol. Eng.* **2010**, *15*, 852–858. [[CrossRef](#)]
29. Biancamaria, S.; Bates, P.D.; Boone, A.; Mognard, N.M. Large-scale coupled hydrologic and hydraulic modelling of the Ob river in Siberia. *J. Hydrol.* **2009**, *379*, 136–150. [[CrossRef](#)]
30. Grimaldi, S.; Li, Y.; Walker, J.P.; Pauwels, V.R.N. Effective Representation of River Geometry in Hydraulic Flood Forecast Models. *Water Resour. Res.* **2018**, *54*, 1031–1057. [[CrossRef](#)]
31. Chow, V.T. *Open Channel Hydraulics*; McGraw-Hill Book Company, Inc.: New York, NY, USA, 1959; ISBN 007085906X 9780070859067.
32. De Doncker, L.; Troch, P.; Verhoeven, R.; Bal, K.; Meire, P.; Quintelier, J. Determination of the Manning roughness coefficient influenced by vegetation in the river Aa and Biebrza river. *Environ. Fluid Mech.* **2009**, *9*, 549–567. [[CrossRef](#)]
33. Corenblit, D.; Tabacchi, E.; Steiger, J.; Gurnell, A.M. Reciprocal interactions and adjustments between fluvial landforms and vegetation dynamics in river corridors: A review of complementary approaches. *Earth Sci. Rev.* **2007**, *84*, 56–86. [[CrossRef](#)]
34. Shih, S.F.; Rahi, G.S. Seasonal Variations of Manning’s Roughness Coefficient in a Subtropical Marsh. *Trans. ASAE* **1982**, *25*, 116–119. [[CrossRef](#)]
35. Pappenberger, F.; Beven, K.; Frodsham, K.; Romanowicz, R.; Matgen, P. Grasping the unavoidable subjectivity in calibration of flood inundation models: A vulnerability weighted approach. *J. Hydrol.* **2007**, *333*, 275–287. [[CrossRef](#)]
36. Schumann, G.; Matgen, P.; Hoffmann, L.; Hostache, R.; Pappenberger, F.; Pfister, L. Deriving distributed roughness values from satellite radar data for flood inundation modelling. *J. Hydrol.* **2007**, *344*, 96–111. [[CrossRef](#)]
37. De Doncker, L.; Troch, P.; Verhoeven, R.; Bal, K.; Desmet, N.; Meire, P. Relation between resistance characteristics due to aquatic weed growth and the hydraulic capacity of the river Aa. *River Res. Appl.* **2009**, *25*, 1287–1303. [[CrossRef](#)]
38. Werner, M.G.F.; Hunter, N.M.; Bates, P.D. Identifiability of distributed floodplain roughness values in flood extent estimation. *J. Hydrol.* **2005**, *314*, 139–157. [[CrossRef](#)]

